INVESTIGATING THE ANISOTROPIC FEATURES OF PARTICLE ORIENTATION IN SYNTHETIC SWELLING CLAY POROUS MEDIA

Fabien Hubert[1,*], Isabelle Bihannic[2,3], Dimitri Prêt[1], Emmanuel Tertre[1], Benoit Nauleau[1], Manuel Pelletier[2,3], Bruno Demé[4], and Eric Ferrage[1]

[1] Université de Poitiers, CNRS IC2MP-HydrASA UMR 7285, 86022 Poitiers cedex, France
[2] CNRS, Laboratoire Interdisciplinaire des Environnements Continentaux, UMR7360, Vandoeuvre lès Nancy, F-54500, France
[3] Université de Lorraine, Laboratoire Interdisciplinaire des Environnements Continentaux, UMR7360, Vandoeuvre lès Nancy, F-54500, France
[4] Institut Laue-Langevin, 6 rue Jules Horowitz, BP156, F-38042 Grenoble, France

Abstract—The present study investigated the anisotropy in the orientation of particles in synthetic swelling clay media prepared from the sedimentation of particle-sized fractions of vermiculite. The different size fractions (<0.1, 0.1−0.2, 1−2, and 10−20 µm) were chosen because they represent the wide range of particle sizes of swelling clay minerals encountered in natural environments. Small-angle neutron scattering (SANS) and neutron diffraction measurements allowed the characteristic scattering/diffraction features to be derived and the quantitative information about the particle orientation distributions along two directions with respect to the sedimentation plane to be extracted. The results obtained confirmed that the increase in particle size was associated with the development of a random orientation for the particles, whereas the hydration state had a negligible impact on the organization of the porous media. For finer vermiculite particles, the rocking curves demonstrated an anisotropy of the systems that is similar to those reported previously on natural montmorillonite minerals. This result suggests that the location of the layer charge has little or no impact on the anisotropy features of particle orientation. For the coarsest fraction (10−20 µm), quantitative information about the particle orientation revealed that the relative proportion of the isotropic contribution represents up to 85% of the material. The anisotropy in the 2D SANS patterns revealed a pore-network anisotropy that was consistent with the particle size.

Key Words—Dehydration, Hydration, Particle Orientation, Rocking Curve, Small-angle Neutron Scattering.

INTRODUCTION

Understanding the anisotropic features of clay-particle orientation and the associated pore morphology is of prime importance in numerous natural environments (*e.g.* rocks or soils) and engineered materials (*e.g.* geomembranes and drilling fluids), where these minerals control both the physical and chemical properties of the systems (Czurda, 2006 and references therein; Harvey and Lagaly, 2006; Prêt *et al.*, 2010a, 2010b; Tertre *et al.*, 2011a, 2011b). Indeed, the presence of these lamellar minerals and the associated development of anisotropy in the organization of the pore network has a considerable impact on the directional dependence of hydraulic permeability, which results in the preferential transfer of fluids and solutes (Vasseur *et al.*, 1995), and on the elastic properties in natural environments (Johansen *et al.*, 2002, 2004; Lonardelli *et al.*, 2007; Voltolini *et al.*, 2009). Furthermore, some clay systems present a swelling/shrinking behavior which results from the hydration/dehydration process. This behavior is responsible for numerous problems in civil engineering and soil science because the shrinkage effect can strongly affect the mechanical properties of the material and generate additional preferential pathways for the transfer of water or contaminants (Tessier *et al.*, 1992; Harris *et al.*, 1994).

When swelling clay minerals such as smectite or vermiculite are present, all of these effects are particularly enhanced because of their large specific surface area and their ability to adsorb water onto their crystal surfaces. As a function of water activity (de la Calle *et al.*, 1978; Ferrage *et al.*, 2010, 2011 and references therein), the swelling of the crystal structure is best revealed by the step-wise increase of the layer-to-layer d_{001} distance from a value of ~10 Å for the dry state to roughly 12.5 Å for the so-called monolayer state and then to ~15.0 Å for the bilayer state (Figure 1a).

Due to their platelet shape, swelling clay particles have a natural tendency to stack parallel to the sedimentation plane. Such preferential particle orientation is usually assessed from experimental rocking curve (RC) measurements on Bragg reflections using X-ray or neutron diffraction, which typically display a pseudo-Gaussian shape. Based on the width of experimental RCs, several studies have shown that the decrease of particle size (Ross and Hall, 1980; Hall *et al.*, 1983) or water content (Inigo *et al.*, 2000) as well as the increase of bulk density (by compression) (Perdigon-Aller *et al.*,
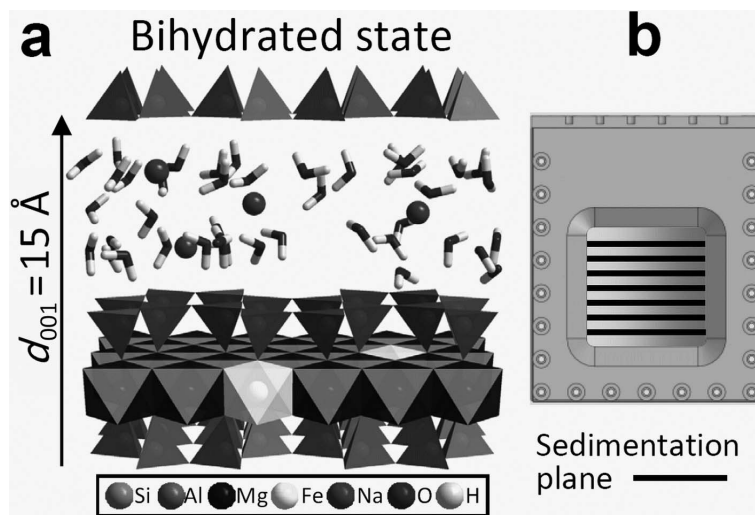
Figure 1. (a) Structure of bihydrated vermiculite. (b) Sample cell designed for neutron scattering/diffraction experiments on the D16 instrument of the Institut Laue-Langevin (Grenoble, France). The sample is inserted in such a way that the sedimentation plane of the particles is perpendicular to the cell surface.

2005, 2007) improved the preferential orientation of clay particles. In contrast, the sample preparation method and the nature of the interlayer cation were shown to have limited influence (Cebula *et al.*, 1979; Hall *et al.*, 1983) though both of those sets of authors suggested that a swelling clay-particle arrangement was more complex and that the wide range of swelling clay-particle arrangements could not be described fully from the simple variation of the width of the RC. Indeed, those authors considered a very low, intense, flat 'background' in addition to the repeatedly described Gaussian distribution. This flat 'background' was interpreted by the presence of a very limited isotropic contribution resulting from particles having random orientation (Cebula *et al.*, 1979; Ross and Hall, 1980; Hall *et al.*, 1983). Highlighting and quantifying such isotropic contribution in oriented swelling clay media is of prime importance owing to its expected significant influence on the physical properties as well as on fluid or solute transfers.

As far as RC analysis on Bragg reflections is concerned, the information obtained is strictly limited to the anisotropic features of swelling clay crystals/ particles. Additional insights can be obtained from small angle X-ray or neutron scattering (SAXS or SANS, respectively). These techniques are sensitive to the crystal−pore interface only and can, thus, reveal the anisotropic features of the pore network. Previous studies devoted to SAXS or SANS measurements indicated that water-content decrease (*e.g.* Méheust *et al.*, 2007) or an increase in the sample compaction (Knudsen *et al.*, 2004) increased the anisotropy of the crystal−pore interface in agreement with results derived from RC analyses. However, apparently no study has performed both SAXS/SANS and RC analyses on the

same sample. Although the anisotropy of the crystal−pore interface is probably governed by the mutual arrangement of particles which have their own orientation, a close relation between results obtained from SAXS/SANS and RC analyses remains to be demonstrated experimentally for swelling-clay porous media.

In the general context of understanding fluid-transfer anisotropy in natural media or engineered materials, the present study aimed to obtain information concerning orientational properties of particles in simplified model systems for swelling-clay porous media. To achieve this objective, different porous media were obtained using particle-sized fractions prepared from the sonication of mm-sized, high-charge vermiculite monocrystals. This allowed the range of particle sizes to be enlarged while maintaining strictly constant crystal chemistry for the different size fractions (Perez-Maqueda *et al.*, 2001; Wiewióra *et al.*, 2003; Perez-Maqueda *et al.*, 2004; de Haro *et al.*, 2005). This coupled approach using a neutron-based scattering/diffraction method was employed for characterizing the particle orientation as well as the associated morphology of the crystal−pore interface in the samples. This non-invasive technique has the advantage of being able to penetrate large samples and the patterns obtained were thus characteristic of the entire bulk material (Bihannic *et al.*, 2009). Experimental RCs were analyzed to derive quantitative information about the particle-orientation distribution as a function of the particle size and hydration state. The possible presence of an isotropic contribution in the samples was checked carefully to provide a strategy for its quantification. The results obtained were then used to interpret qualitatively the experimental small-angle neutron scattering patterns with a view to linking the orientational dependence of particles and crystal−pore interfaces.

MATERIALS AND METHODS

Material description

The swelling clay sample investigated in the present study was a natural vermiculite from Santa Olalla (Huelva, Spain) resulting from alteration of well crystallized phlogopite (González García and García Ramos, 1960; de la Calle *et al.*, 1977). The structural formula is (Marcos *et al.*, 2003; Arguelles *et al.* 2010): $[(Mg_{4.92}Fe_{0.44}Al_{0.60}Ti_{0.04})(Si_{5.66}Al_{2.34})O_{20}(OH)_4]M_{1.64}^+$. This vermiculite was originally Mg-saturated and exhibits an important tetrahedral charge deficit resulting from Al-for-Si substitutions (Figure 1a).

Preparation of selected particle size samples

Pluri-centimetric vermiculite monocrystals were first transformed into $1-4$ mm flakes by knife-milling followed by dry sieving. The flakes were then immersed in hydrochloric acid (1 g of sample in 20 mL of 10^{-4} mol L^{-1} HCl solution for 5 min) to dissolve carbonates and then washed three times in distilled water. Most of the sub-millimetric oxides were finally removed from the suspension using a magnetic stick.

The purified $1-4$ mm flakes were sonicated using a high-intensity ultrasonic titanium-tipped disruptor horn (13 mm diameter, Sonics and Materials, Newtown, Connecticut, USA) operating at 750 W output with a 20 kHz converter. The tip of the horn was dipped into a cylindrical glass tube (4 cm diameter) containing 3 g of the vermiculite flakes in 50 mL of distilled water (Perez-Maqueda *et al.*, 2001; Wiewióra *et al.*, 2003; Perez-Maqueda *et al.*, 2004; de Haro *et al.*, 2005). During the 10 h of sonication, the temperature of the solution was maintained at ~30ºC using a cylindrical jacket cooling cell. This procedure was applied to a total of 128 g of the initial $1-4$ mm flakes to obtain a sufficient amount of the sonicated stock suspension before particle-size separation.

Four particle-size fractions were chosen in the present study: $10-20$, $1-2$, $0.1-0.2$, and <0.1 μm. These size fractions were chosen because they represent the wide spectrum of particle sizes that are encountered for swelling clay minerals in natural media (Dixon and Weed, 1989; Caillaud *et al.*, 2009; Hubert *et al.*, 2012). The separation process was adapted for each fraction to obtain the most restricted particle-size distribution. The >50 μm particles were first removed from the stock suspension by wet-sieving. The three finer fractions (*i.e.* <2 μm) were then separated sequentially using a Biofuge stratos centrifuge (Heraeus, Hanau, Germany) starting from the finest (<0.1 μm) particles. To perform this step, ~6 g of the <50 μm clay fraction was dispersed in 300 mL of water, and five centrifugation cycles were used to extract the <0.1 μm fraction until the supernatant became clear. A second cycle of centrifugation was performed on the <0.1 μm suspension obtained to recover the remaining coarser particles (>0.1 μm) that

were placed back into the stock suspension. After this procedure was applied to the complete stock suspension, the $0.1-0.2$ μm and then the $1-2$ μm fractions were obtained using the same separation method. In the case of the last $10-20$ μm fraction, separation was achieved by settling (at 20ºC) the dispersed residual stock $2-50$ μm material in a glass column and by siphoning the <10 μm and >20 μm particles according to Stoke's law.

Finally, all of the fractions were re-concentrated through the evaporation of water and then Na-saturated using five saturation cycles in a 3 mol L^{-1} NaCl solution. The fractions were then washed in distilled water using the dialysis procedure.

Specific surface area measurements from N_2 adsorption-desorption isotherms

Classical N_2 adsorption-desorption isotherms were obtained at 77 K using a lab-built automatic step-by-step volumetric adsorption apparatus (Nancy, France; for the experimental setup; for details see Montarges-Pelletier *et al.* (2005)). For each fraction, a sample mass of ~1 g of powder was first out-gassed under a residual pressure of 0.01 Pa at 150ºC for 18 h before the N_2 adsorption-desorption measurements. The surface areas were determined for each fraction (Table 1) using the BET method ((Brunauer *et al.*, 1938), AFNOR NF X 11-621).

Sample cells designed for neutron scattering/diffraction experiments and preparation of synthetic porous media

Flat, home-made cells were designed to obtain scattering/diffraction patterns from the synthetic porous media under controlled-humidity conditions (Figure 1b). These cells are composed of two open rectangular aluminum parts where quartz windows (3 cm × 3 cm, 2 mm thick) are attached, and an additional aluminum flat rectangular piece (5.8 cm × 1.4 cm, 3 mm thick) ensured the top sealing. The three pieces were connected using 37 screws, and the internal volume was isolated from the surrounding atmosphere using Teflon® seals. Once completely assembled, the external cell dimensions were 7.2 cm × 5.8 cm with a thickness of 14 mm, and the internal dimensions available for the clay porous media were 5.5 cm × 3 cm and 3 mm thick. The elongated internal dimension was chosen to allow the porous medium to hydrate or dehydrate under the controlled-humidity conditions while maintaining a constant illumination of the sample through the quartz windows.

The swelling clay media were prepared from sedimented clay-particle aggregates. For the three finest (<0.1, $0.1-0.2$, and $1-2$ μm) clay fractions, 10 mL aliquots of the suspension (at a concentration of 20 g of clay per kg of water) were poured through a Millipore filter (0.4 μm). The resulting clay films (3.7 cm in diameter) were then cut with a razorblade to obtain thin sticks with surface dimensions of ~2.8 cm × 0.25 cm. Hundreds of such flat specimens were stuck together

Table 1. Specific surface areas of the different particle-size fractions and evolution of the 001 reflection qualitative descriptors (position, width, and intensity ratio between the $q_{//}$ and $q_{\perp}$ directions) as a function of the hydration state.

Sample	S_{BET} (m²/g)	Hydration state	— d_{001} (Å) —		FWHM (Å⁻¹)		$I_{max}\,(q_{//})/I_{max}\,(q_{\perp})$ (%)
			$q_{//}$	$q_{\perp}$	$q_{//}$	$q_{\perp}$	
<0.1 μm	146	2W	−	14.9	−	0.041	0
		0W	−	10.5	−	0.106	0
0.1−0.2 μm	120	2W	−	14.8	−	0.030	0
		1W	−	12.2	−	0.069	0
		0W	−	10.1	−	0.058	0
1−2 μm	16	2W	14.8	14.9	0.017	0.018	9
		1W	12.2	12.1	0.023	0.023	9
		0W	9.8	9.9	0.024	0.025	8
10−20 μm	<1	2W	14.9	15.0	0.016	0.019	36
		1W	11.8	11.9	0.016	0.017	17
		0W	9.9	9.9	0.025	0.024	22

face-to-face by successive deposition of a drop of water between the flat surfaces of two neighboring specimens to obtain a final rigid cake 4.5 cm thick (normal to the sedimentation plane in Figure 1b) that was placed in the designed cell. For the 10−20 μm size fraction, because of the limited particle−particle cohesion, the particles were settled sequentially directly in the cell. This process was achieved by using several cycles of sedimentation of an aliquot of the suspension and removing the remaining supernatant before finally equilibrating at room relative humidity (RH).

Because of the amounts of material obtained for the different fractions, two cells were prepared for the 0.1−0.2, 1−2, and 10−20 μm size fractions, and only one cell was prepared for the <0.1 μm particle size fraction.

SANS and neutron diffraction experiments

Experimental setup and data acquisition. Small-angle neutron scattering/diffraction experiments were performed on the cold-neutron small-momentum transfer diffractometer D16 at the Institute of Laue-Langevin (Grenoble, France). This instrument has a graphite monochromator that provides an incident neutron beam with a wavelength (λ) of 4.75 Å and a 2D position-sensitive ³He detector.

Three different configurations were used to collect the SANS patterns, high-angle θ/2θ scans and ω scans (rocking curves). For all configurations, the following angles are defined: θ, where 2θ is the angle between the incident and diffracted beam and ω is the angle between the normal of the incident beam and the surface of the cell (Figure 2). (1) For SANS measurements (Figure 2a), the cell was positioned perpendicular to the incident beam, which resulted in zero values for θ and ω. This configuration allowed the collection of 2D SANS patterns in the $0.026<q<0.188$ Å⁻¹ q range (where q is the modulus of the scattering vector, $q = 4\pi\sin(\theta)/\lambda$). (2)

Conventional neutron diffraction (ND): θ/2θ scans were performed in transmission geometry by rocking the sample by an angle θ (ω = θ, Figure 2b) with respect to the incident beam and by scanning the detector position to collect the associated 2θ intensities. The corresponding q values ranged between 0.094 and 2.220 Å⁻¹, with a resolution of 0.003 Å⁻¹. (3) Rocking curves (RC) were collected with the detector positioned in θ/2θ geometry corresponding to the 001 reflection, which allowed the sample to rotate through the angle ω with respect to the normal of the incident beam (Figure 2c). With this setup, the ω scans were performed in the range −50<ω<70° in transmission geometry.

Except for the <0.1 μm fraction, three characterizations were performed for the different particle size fractions, where each corresponds to the analysis of the three common hydration states known for swelling clay minerals (*i.e.* the bihydrated, 2W; monohydrated, 1W; and dehydrated, 0W, states (Ferrage *et al.*, 2005a, 2005b)) following the water-vapor desorption pathway. To obtain these hydration states, the sample cells were opened, and one of the two cells was equilibrated for a period of 1 week at RH = 98% using a $CuSO_4$ saturated salt solution, whereas the other cell was maintained at room humidity over the same time interval (RH ≈35%). The first and second conditions are expected to produce the 2W and 1W states, respectively. The 0W state was prepared by drying the sample that was initially equilibrated at the 1W state in an oven at 105°C under primary vacuum conditions (~10⁻³ Pa). In the case of the <0.1 μm size fraction, the unique sample cell was first equilibrated in the 2W state and then dried to obtain the 0W state, following the same procedure as described above.

For all samples (with different particle sizes and hydration states), the sample cell was placed on a sample holder to record SANS, ND, and RC scans in two directions with respect to the sedimentation plane by

rotating the sample cell by 90° (Figure 3). Note that in the case of ND analysis and for a clay sample with particles aligned flat with respect to the sedimentation plane, these two directions, hereafter referred to as $q_{//}$

(when the sedimentation plane is parallel to the diffraction plane) and $q_{\perp}$ (when the sedimentation plane is perpendicular to the diffraction plane) correspond to the analysis of the $hk0$ and $00l$ reflections, respectively.
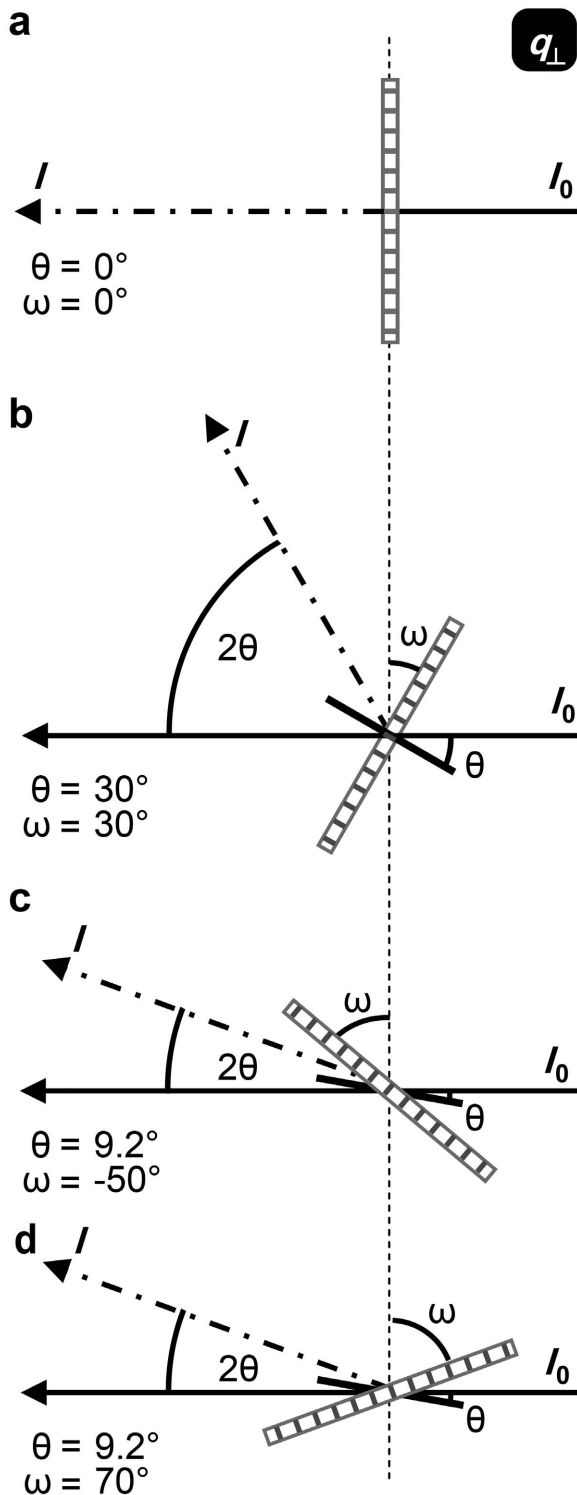
Treatment of experimental data. Data processing was performed using two different procedures depending on the experimental configuration (SANS and diffraction on the one hand, rocking curves on the other).

(1) For the SANS and $\theta/2\theta$ ND scans, the background originating from the sample holder was subtracted from each 2D pattern after correcting for the transmission. The transmission, T, was evaluated by measuring the total intensity (I) through the sample and the intensity through the sample holder alone (I_0) in the configuration where $\theta = \omega = 0$:

$$T = I/I_0 \tag{1}$$

The scattered intensity, which was divided by the transmission and then corrected for the sample-holder contribution, was converted to absolute units by normalization over water as a standard. The 1D radial distribution curves, $I_c(q)$, were then extracted from the merged 2D patterns which resulted from the regrouping of the signal over a 16° angular sector. Finally, for the hydrated samples, the incoherent signal due to water was estimated from the flat background intensity in the 0.8 to 2 Å^{-1} q range, and this constant value was then subtracted from the whole pattern.

(2) For RC measurements, the 2D pattern recorded for each position of ω angle was treated independently. Indeed, for each pattern, a radial distribution function ($I(q)$) was extracted by averaging the signal over a 10° horizontal angular sector centered on the beam center. The area under the Bragg peak was then integrated after the subtraction of a linear background. For this non-symmetrical $\theta/2\theta$ mounting, the beam attenuation is a function of ω. Consequently, each integrated intensity must be multiplied by the non-symmetric attenuation factor ($A_{\text{n.sym}}$) (Drits and Tchoubar, 1990):

$$A_{\text{n.sym}} = \frac{K_a}{x_o} \times \frac{\sin(90-\omega) - \sin(90-\omega+2\theta)}{\sin(90-\omega+2\theta)} \times$$
$$\frac{1}{\exp(-K_a/\sin(90-\omega)) - \exp(-K_a/\sin(90-\omega+2\theta))} \tag{2}$$

Figure 2 (*left*). Illustration of the experimental geometries used for (a) small-angle, (b) neutron diffraction, and (c) Rocking Curve experiments and associated definition of the angle ω (between the normal of the incident beam and the surface of the cell) and the angle θ (between the incident beam and the normal of the cell surface). For SANS experiments, $\theta = \omega = 0$, whereas for neutron diffraction ($\theta/2\theta$ scans), $\theta = \omega \neq 0$. Gray bars represent the sedimentation plane, whereas the solid black line corresponds to the particle in Bragg conditions.
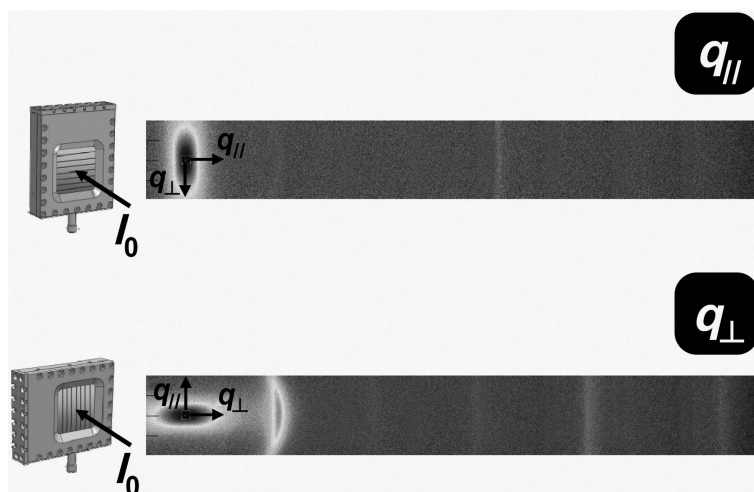
Figure 3. The D16 instrumental setup for recording scattering/diffraction patterns and rocking curves in the directions parallel ($q_{//}$) and perpendicular ($q_\perp$) to the sedimentation plane (2D experimental data are the small-angle and neutron diffraction patterns of the $0.1-0.2$ μm fraction in the bihydrated state).

where K_a represents the absorption coefficient ($K_a = -\ln(T)$) and x_0 is the thickness of the sample. Note that this expression, which is used to correct the intensity for absorption ($I_c(\omega)$), is only valid in the case of the ω range investigated in the present study because the geometry remains in the transmission mounting throughout the entire RC measurement.

RESULTS AND DISCUSSION

Qualitative analysis of 1D patterns

The experimental SANS/ND patterns are presented for the different size fractions as a function of the hydration state (Figure 4). As shown for the $q_\perp$ direction, the profiles obtained displayed a typical shift in the d_{001} values as a function of dehydration. Indeed, the d_{001} obtained (Table 1) exhibited values for all size fractions at ~14.90±0.10, ~12.05±0.15, and ~10.1±0.2 Å for the bihydrated, monohydrated, and dehydrated states, respectively.

For the monohydrated state, room RH (~35%) corresponds to the humidity where the two types of monohydrated layers can coexist (at 11.9 and 12.2 Å, respectively (de la Calle *et al.*, 1985)) which probably contributes to the variability in the d_{001} values. Regarding the dehydrated state, the presence of additional bumps on the low-angle side of the 001 reflection for the <0.1 and $0.1-0.2$ μm fractions (Figure 4) indicates the remaining presence of layers that have higher hydration states. This feature is attributed to a slight dissolution of vermiculite during the washing process performed by dialysis that resulted in the reincorporation of Mg cations into the interlayer space (Tertre *et al*, 2013). This dissolution was probably enhanced for the finer fractions because of their increased specific surface areas (Table 1). These layers

probably contributed to the increased d spacing values for the two finest fractions and to the overall variability in the d_{001} values.

As a general trend and for a given hydration state, the full width at half-maximum (FWHM) intensity values measured on the entire 001 reflections increase with decreasing particle size (Table 1). This feature is related to the decrease of the coherent scattering domain size for the finest fractions (Drits *et al.*, 1997). Note that the very close values obtained for the $1-2$ and $10-20$ μm fractions can be attributed to the instrumental resolution that limits the minimum detectable width variation (Cebula *et al.*, 1979), as additional X-ray diffraction analyses showed a clear variation in peak width for these two samples (data not shown). In addition, two reasons may account for the observed increase of the FWHM values with decreasing hydration state (Table 1, Figure 4) for a given sample. First, even though the interlayer spaces are mostly Na-saturated, the proportion of interlayers with Mg cations for the finest fractions probably remained in the bihydrated state throughout the entire experiment (de la Calle and Suquet, 1988). Consequently, the contrast between the d spacing of the Mg- and Na-interlayers increases with decreasing hydration state. According to Mering's rule (Méring, 1949), this structural feature induces an additional broadening of the 001 and other 00l reflections (Figure 4). Second, a reduction of the thickness of the layer during dehydration can lead to the generation of additional intra-crystalline porosity that induces a disruption of the periodic layer stacking and, thus, reduces the sizes of the coherent scattering domains.

The 1D patterns in the $q_{//}$ direction exhibit 00l reflections for the two larger fractions, whereas only $hk0$ (*i.e.* 02l,11l) reflections are observed for the <0.1 and $0.1-0.2$ μm samples (Figure 4). In addition, the ratio
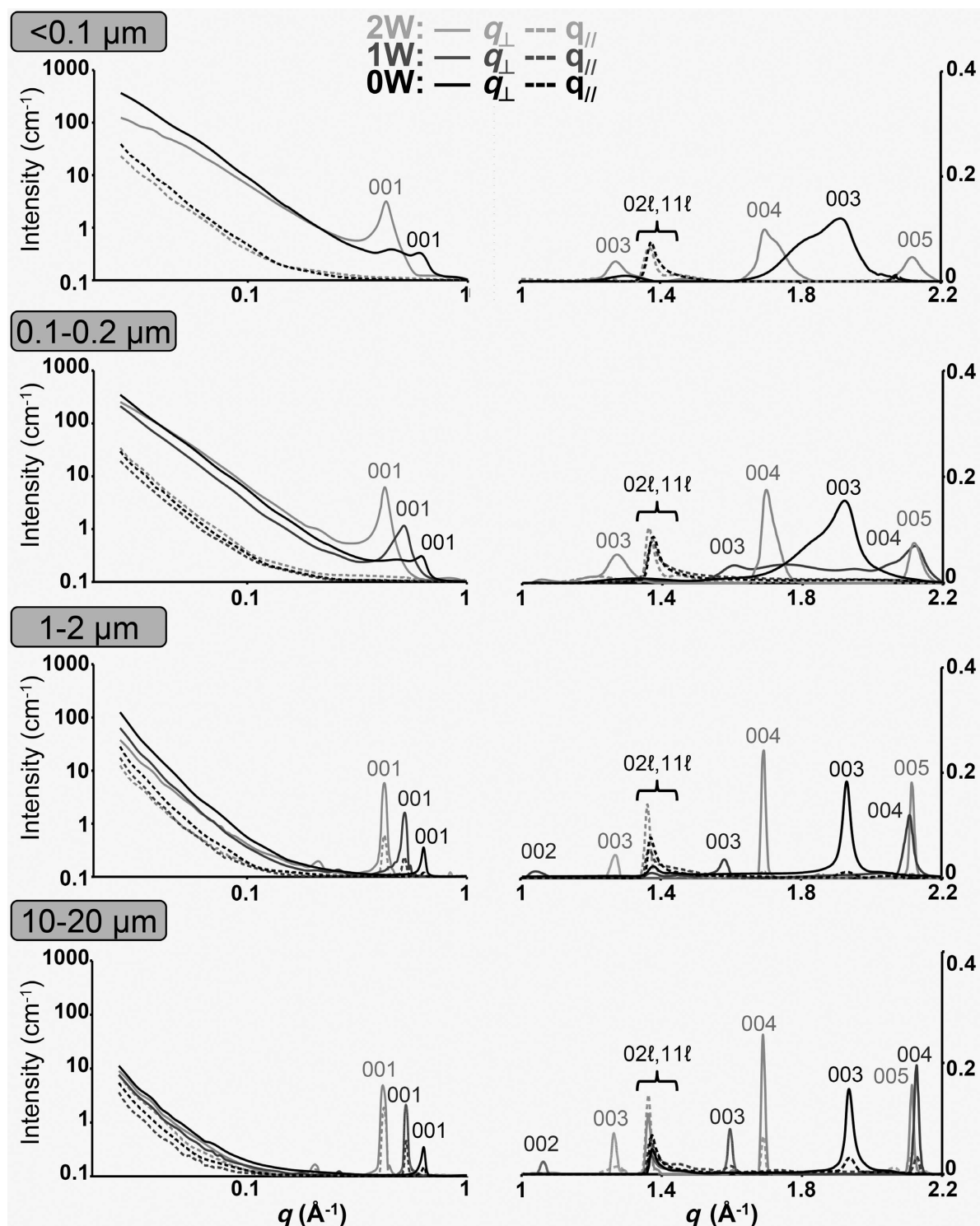
Figure 4. 1D scattering/diffraction intensities (in cm^{-1}) recorded for the different particle size fractions. Profiles obtained in the perpendicular ($q_\perp$) and parallel ($q_{//}$) directions to the sedimentation plane are shown with solid and dotted lines, respectively. For the low-q region (between 0.026 and 1 Å^{-1}), the x and y axes are expressed in log units. Profiles for bihydrated (2W), monohydrated (1W), and dehydrated (0W) states are shown in light gray, gray, and black, respectively.

between the maximum intensity of the 001 reflections obtained in the $q_{//}$ over $q_{\perp}$ direction range between ~20 and 40% for the 10−20 μm fraction and is ~10% for the 1−2 μm samples (Table 1). This evolution reveals interesting features concerning the orientation of the particles in the samples with varying particle size. Indeed, for coarser fractions, the presence of 00*l* reflections in both the $q_{//}$ and the $q_{\perp}$ directions indicates that the porous media have partly disoriented particles. In contrast, a zero $q_{//}/q_{\perp}$ ratio for the finest fractions can be interpreted as a well oriented preparation. However, the information extracted from the $q_{//}/q_{\perp}$ ratio is very limited concerning the particle orientation because it only provides an estimate of the relative proportion of particles along these two extreme directions (*i.e.* along $q_{//}$ and $q_{\perp}$) but cannot allow the determination of the actual distribution of particle orientation around these two directions. This latter information is best revealed by quantitative analysis of the rocking curves, as performed below.

Quantitative analysis of particle orientation from ω scans

Sample geometry. Each sample consists of an assembly of individual particles, the orientation of which may be described through their normal, $\vec{n}$, which is a unit-length vector that is perpendicular to the basal surface of the particle. In addition, the entire material may be described by a unit vector, $\vec{n}_s$, which is perpendicular to the sedimentation plane. The angle α is defined as the angle between $\vec{n}$ and $\vec{n}_s$ (Figure 5a). This angle denotes the orientational deviation of each particle with respect to the sedimentation plane. The acquisition consists of measuring the intensity of the 001 Bragg peak as a function of ω, which defines the position of the sample relative to the beam (see the section 'Experimental setup and data acquisition'). For a particular value of ω, only particles satisfying the Bragg conditions (particles oriented with an angle θ with respect to the incident beam) will contribute to the signal (Figure 5a). From these geometrical considerations, it follows for experimental RC measurements performed in the $q_{\perp}$ direction that α = ω-θ.

Fitting strategy for quantitative analysis. As an illustration, the fitting strategy used for the analysis of the RC experimental data is shown for the 1−2 μm fraction in the bihydrated state (Figure 6). From the integrated intensity below the 001 reflection in the $q_{\perp}$ direction, the absorption correction using equation 2 leads to a symmetrization of the ω-scan intensities with a maximum intensity located at ω = θ (*i.e.* the Bragg position for the 001 reflection, Figure 6a).

Because of instrumental constraints, the accessible α values range between −60 and 60°, whereas for RC analysis the required range of α angles is between −90 and 90°. Consequently, an extrapolation of the experi-
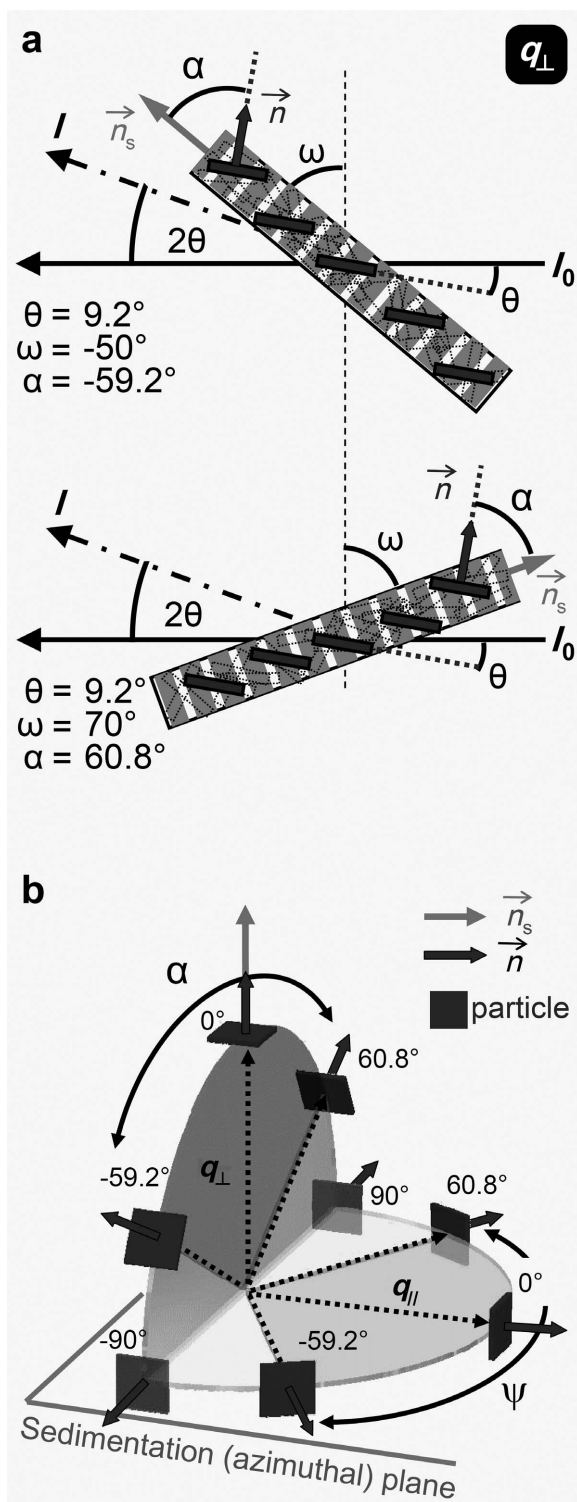

Figure 5. (a) Illustration of the geometry of particles and sample during the rocking-curve measurements. (b) Three-dimensional schematic of the orientation of the particles investigated through rocking-curve experiments according to the $q_{//}$ or $q_{\perp}$ directions and respective accessible values for α and ψ angles. Particles are represented by dark gray squares. Light gray angular sectors correspond to inaccessible α and ψ angle values.
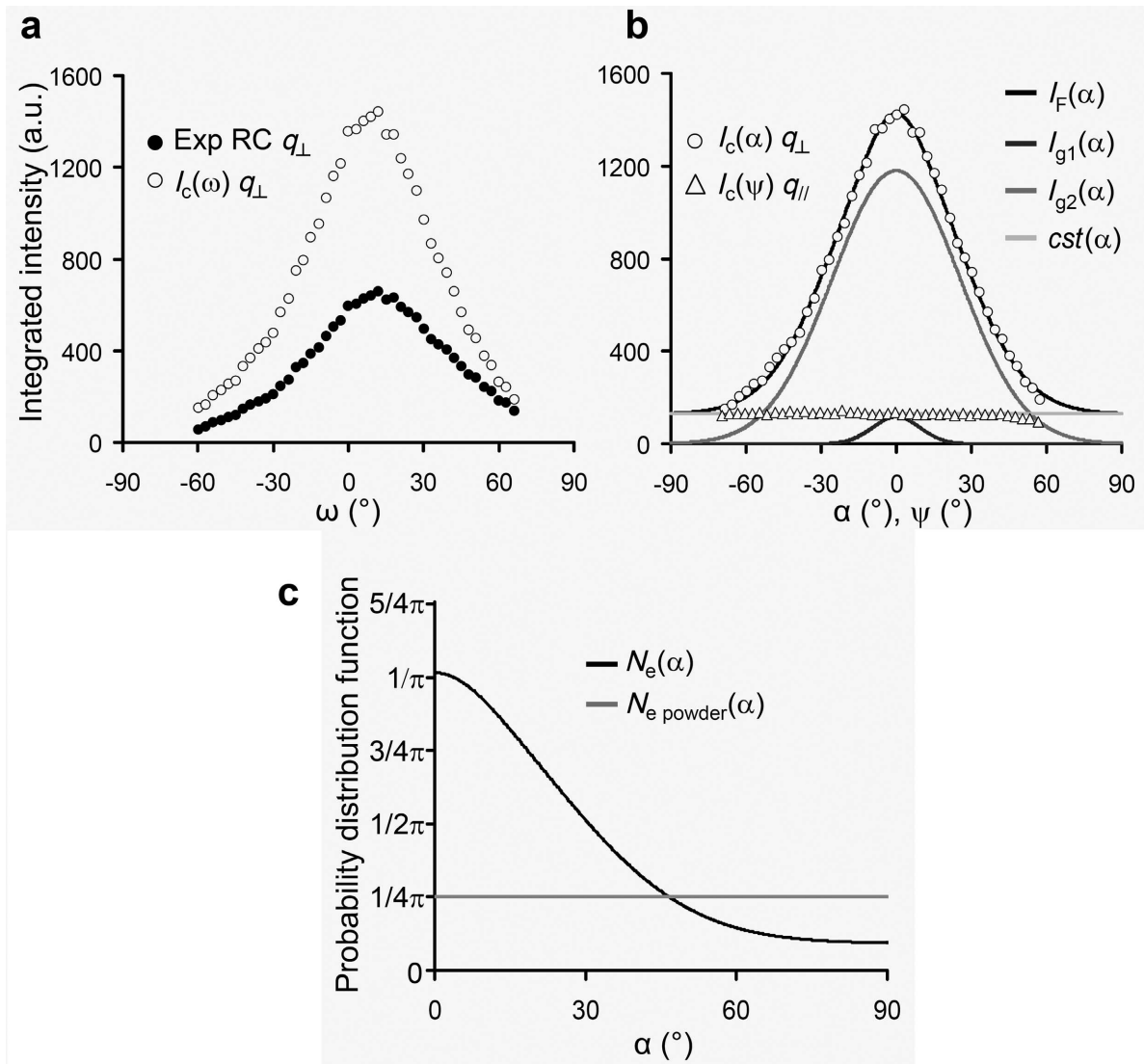
Figure 6. Fitting strategy for the quantitative analysis of the particle orientation. (a) Correction of the experimental intensities (Exp RC) from sample absorption leading to a symmetrization of the ω scans ($I_c(\omega)$). (b) Decomposition of the experimental rocking-curve intensities obtained in the parallel ($q_{//}$) and perpendicular ($q_\perp$) directions (see Figure 5b) on the basis of two Gaussian functions ($I_{g1}(\alpha)$ and $I_{g2}(\alpha)$) and a constant background (cst(α), see text for details). (c) Orientation distribution function $N_e(\alpha)$.

mental data is necessary (Drits and Tchoubar, 1990), which is performed here using a best-fit approach with symmetrical functions. These geometrical constraints are illustrated in Figure 5b, where the α range available for the RC measurements corresponds to the gray angular sector centered on the $q_\perp$ direction. The RCs recorded after rotating the sample cell by an angle of π/2 allow the orientation of the particles relative to the $q_{//}$ direction to be probed. For particles with a uniaxial symmetry, the intensity of the Bragg peak recorded in this configuration should be a constant as a function of the azimuthal angle, ψ (Figure 5b).

All attempts to reproduce the experimental data using a single Gaussian function (Reynolds, 1986; Dohrmann

et al., 2009) were unsuccessful. Similarly, the consideration of one Gaussian and a flat background, as done by Cebula et al. (1979), did not reproduce satisfactorily the experimental profiles. For all experimental data obtained here in the $q_\perp$ direction, the best fit of the RC absolute intensities as a function of α ($I_F(\alpha)$) was obtained by assuming two Gaussian distributions (i.e. g1 and g2) and a constant contribution (i.e. cst):

$$I_F(\alpha) = I_{g1}(\alpha) + I_{g2}(\alpha) + \text{cst}(\alpha) \qquad (3)$$

This model allows us to reproduce the complete set of RC intensities (Figures 6b, 7). The constant contribution is assigned to a certain number of particles that have a random orientation as suggested by Cebula et al. (1979),
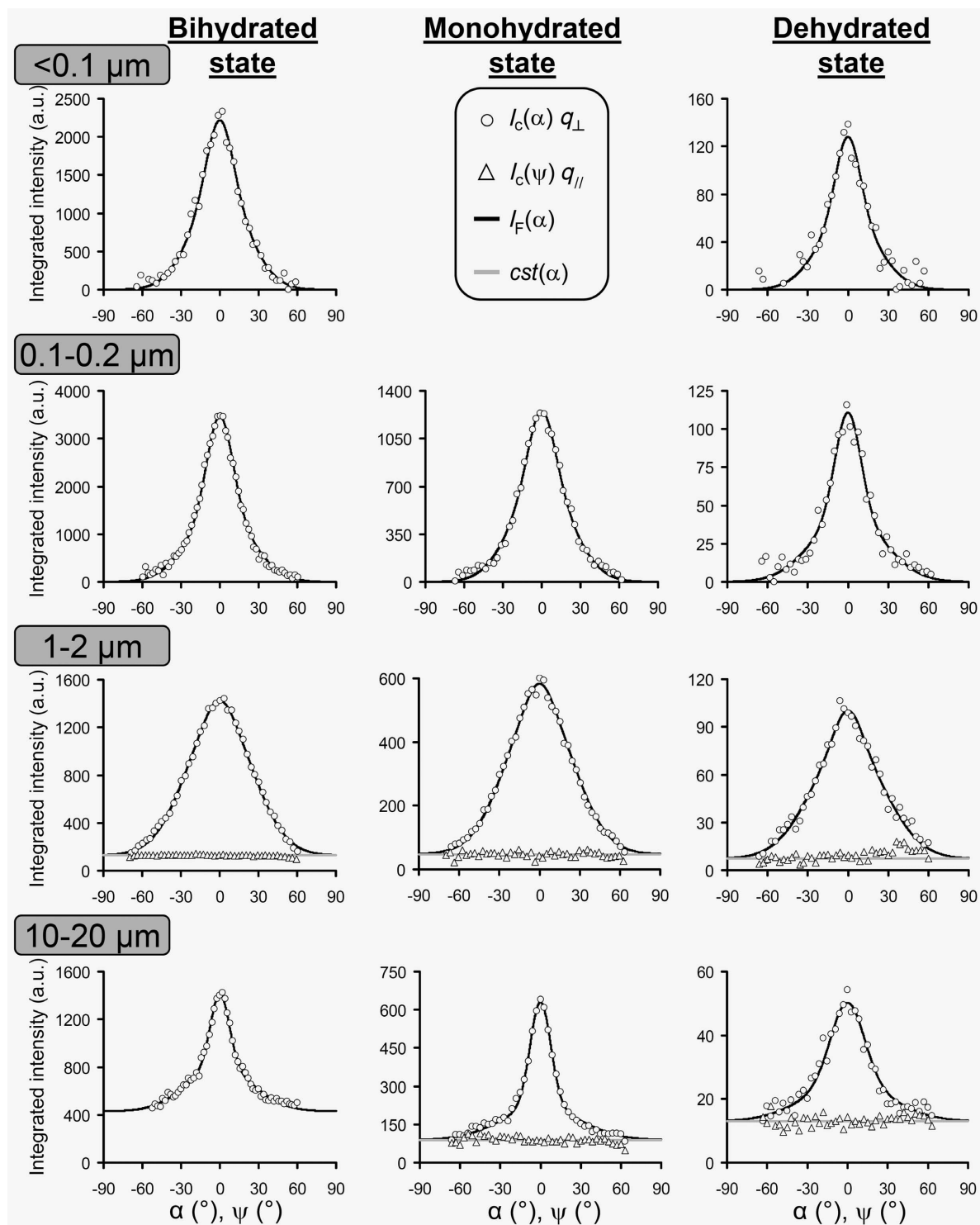
Figure 7. Experimental rocking-curve intensities obtained in the $q_\perp$ direction and associated fits for the different particle size fractions in the bihydrated (2W), monohydrated (1W), and dehydrated (0W) states. For some samples, the experimental profiles obtained in the $q_{//}$ direction are shown.

whereas the two types of Gaussians can be viewed as a reminiscence of the two types of anisotropic contributions assumed by Hall *et al.* (1983). The difference between these two anisotropic contributions was attributed to the better dispersion of finest particles in comparison with coarser ones (Hall *et al.*, 1983). Indeed, the better

dispersion of finest particles in their <0.05 μm fraction of Na-montmorillonites (Hall *et al.*, 1983) led to a RC in which a sharp peak was superimposed on a wide curve. In addition, the latter model permits a comparison of the FWHM values obtained with those reported in the literature for other swelling clay minerals (Cebula *et al.*, 1979; Hall *et al.*, 1983).

Note that the approach proposed by Méheust *et al.* (2006) using the Maier-Saupe equation to fit the orientation distribution functions from two-dimensional wide-angle scattering of X-ray (WAXS) patterns has also been tested (data not shown). This approach could allow fitting of the RC data as well as orientation distribution functions extracted from 2D SANS patterns using only one parameter, m, that provides the degree of anisotropy of the particle organization. However, despite interest in this approach to help assess the particle organization, the Maier-Saupe equation fails to reproduce the complex shape of the RC when a sharp peak is superimposed on a wide curve as obtained for RC of a 10−20 μm fraction. Therefore, such an approach has not been used and quantitative analysis of particle organization has been performed by applying the decomposition method from Cebula *et al.* (1979) and Hall *et al.* (1983).

To assess the validity of the isotropic nature of the flat contribution, the same RC was collected by turning the sample holder in the $q_{//}$ direction. Thanks to the same illuminated volume in both the $q_{//}$ and the $q_\perp$ directions (Figure 6b), the constant RC intensities in the $q_{//}$ direction match perfectly with the intensities of the cst(α) contribution used to fit the RC patterns in the $q_\perp$ direction (Figures 6b, 7). This finding is logical because the particles analyzed for α = ψ = −90º or α = ψ = 90º (in $q_\perp$ and $q_{//}$ directions, respectively) are strictly identical (Figure 5b). These results reveal two features clearly: (1) the constant evolution of intensity in the $q_{//}$ geometry confirms the uniaxial symmetry of the system (*i.e.* all ψ angles are equiprobable), and (2) the true isotropic nature of the constant contribution considered for the $q_\perp$ direction, which was previously suggested in the literature (Cebula *et al.*, 1979; Ross and Hall, 1980; Hall *et al.*, 1983; Perdigon-Aller *et al.*, 2005, 2007).

From the uniaxial consideration, it follows that the RC data obtained in the $q_\perp$ direction are independent of the azimuthal angle, ψ, and that they fully represent the preferential orientation of the particles in the sample. This result permits description of the orientation of the particles as (Plançon, 1980):

$$dN = N_t N_e(\Omega) d\Omega \qquad (4)$$

where dN is the number of particles with a normal, $\overrightarrow{n}$, contained in $d\Omega$, which is the elementary solid angle. N_t and $N_e(\Omega)$ represent the total number of particles and the orientation distribution function (ODF), respectively. Note that the latter is equivalent to a probability density function and, thus, satisfies the following condition: $\int N_e(\Omega) d\Omega = 1$.

Because of the uniaxial symmetry, $d\Omega$ is expressed as a function of α providing:

$$\int N_e(\Omega) d\Omega = \int_0^\pi I_F(\alpha) 2\pi \sin(\alpha) d\alpha = 1 \qquad (5)$$

By definition, the orientation function for a completely random orientation of particles is expressed as $N_e(\alpha) = 1/(4\pi)$ (Figure 6c). In the case of non-random particle orientation, $N_e(\alpha)$ can be obtained from equations 4 and 5:

$$N_e(\alpha) = I_F(\alpha) / \int_0^\pi I_F(\alpha) 2\pi \sin(\alpha) d\alpha \qquad (6)$$

Put more simply, $N_e(\alpha) = I_F(\alpha)/S$ with $S = \int_0^\pi I_F(\alpha) 2\pi \sin(\alpha) d\alpha$.

By combining equations 4 and 6:

$$\int \frac{dN}{N_t} = \frac{2\pi}{S} \int_o^\pi I_F(\alpha) \sin(\alpha) d\alpha = 1 \qquad (7)$$

Considering the different types of functions used to fit the experimental RCs (equation 3), this equation becomes:

$$\int \frac{dN}{N_t} = \frac{2\pi}{S} \int_o^\pi \left[I_{g1}(\alpha) + I_{g2}(\alpha) + cst(\alpha) \right] \sin(\alpha) d\alpha = 1 \qquad (8)$$

or:

$$\int \frac{dN}{N_t} = \frac{2\pi}{S} \int_o^\pi I_{g1}(\alpha) \sin(\alpha) d\alpha +$$
$$\frac{2\pi}{S} \int_o^\pi I_{g2}(\alpha) \sin(\alpha) d\alpha +$$
$$\frac{2\pi}{S} \int_o^\pi cst(\alpha) \sin(\alpha) d\alpha = 1 \qquad (9)$$

The three terms of this equation correspond to the relative contributions of the different orientation distribution functions. According to equation 4, such relative contributions are the proportions of particles that follow the different orientation distribution functions. These relative contributions, which are referred to as $cont_{g1}$, $cont_{g2}$, and $cont_{cst}$ (Table 2), can then be expressed as:

$$cont_{g1} = \frac{2\pi}{S} \int_o^\pi I_{g1}(\alpha) \sin(\alpha) d\alpha \qquad (10)$$

$$cont_{g2} = \frac{2\pi}{S} \int_o^\pi I_{g2}(\alpha) \sin(\alpha) d\alpha \qquad (11)$$

$$cont_{cst} = \frac{2\pi}{S} \int_o^\pi cst(\alpha) \sin(\alpha) d\alpha \qquad (12)$$

with $cont_{g1} + cont_{g2} + cont_{cst} = 1$.

Table 2. Quantitative analysis of the ω scans recorded in the $q_\perp$ direction as a function of the size fraction and hydration state. The widths of the Gaussian functions are used for the decomposition of the experimental ω scans for the two anisotropic contributions (g1 and g2). The relative proportions of g1, g2, and cst contributions are obtained from equations 10, 11, and 12, respectively (see text for details).

Sample	HS	FWHM$_{exp}$ (°)	Decomposition parameters			Relative contributions		
			FWHM$_{g1}$ (°)	FWHM$_{g2}$ (°)	Rp (%)	cont$_{g1}$ (%)	cont$_{g2}$ (%)	cont$_{cst}$ (%)
<0.1 μm	2W	33	23	51	7.6	14	86	0
	0W	30	21	51	13.7	16	84	0
0.1−0.2 μm	2W	31	23	56	4.5	19	81	0
	1W	36	24	54	6.2	14	86	0
	0W	29	22	62	12.8	17	83	0
1−2 μm	2W	54	22	60	2.8	1	62	37
	1W	51	21	59	3.5	1	63	36
	0W	44	23	64	7.8	3	65	32
10−20 μm	2W	23	17	60	3.7	2	13	85
	1W	22	18	69	4.7	6	24	70
	0W	32	29	74	8.6	7	18	75

HS corresponds to the hydration state of the sample. FWHM$_{exp}$ stands for the full-width at half maximum of the experimental ω scan, whereas FWHM$_{g1}$ and FWHM$_{g2}$ correspond to the width of the two gaussian contributions, respectively, used for the decomposition treatment. The goodness of fit parameter Rp=[($\Sigma(I_{exp}-I_{calc})^2/\Sigma(I_{exp})^2]^{0.5}$ is used to assess the quality of the fit.

Influence of particle size and hydration state on particle orientation. For all samples, the results obtained from the fit of the experimental ω scans (Figure 7) and the associated quantitative analysis are reported in Table 2. This table includes the widths of the experimental profiles (FWHM$_{exp}$) and the respective contributions of the different orientation distribution functions (cont$_{g1}$, cont$_{g2}$, and cont$_{cst}$).

The comparison between the contributions of the anisotropic and isotropic orientation distribution functions obtained for the different fractions demonstrate clearly an increase in the proportion of the isotropic contribution with increasing particle size (Table 2). This contribution is indeed absent from the two finer fractions, whereas it increases from 32−37% to 70−85% for the 1−2 and 10−20 μm fractions, respectively (Table 2). Such a contribution, revealed by the presence of a background in experimental ω scans, has been reported by Cebula *et al.* (1979) and Hall *et al.* (1983) in the case of montmorillonite samples saturated with monovalent cations. Regarding the anisotropic contributions, the experimental widths of the RCs collected between 29 and 54° for the two finest fractions are fully consistent with those obtained previously. Indeed, Cebula *et al.* (1979) reported an experimental width near 40° for a natural non-fractionated montmorillonite saturated with different monovalent cations, whereas Hall *et al.* (1983) obtained FWHM values ranging between 23 and 65° for different size-fractionated <2 μm Na-montmorillonites. Furthermore, in the case of a <0.05 μm fraction, these latter authors decomposed their experimental ω-scan profiles in terms of a narrow and a broad Gaussian

distribution, the widths of which (~25° and ~50°, respectively) were very similar to those used in the present study to fit the entire set of experimental RCs (22±3° and 60±7° for g1 and g2, respectively, Figure 7, Table 2). When comparing the results obtained for the <0.1 and 0.1−0.2 μm fractions, the relative proportions for the g1 and g2 contributions (Table 2) and the FWHM values obtained for the g1 function are similar for both samples. However, a small increase in the FWHM value for the g2 contribution of the 0.1−0.2 μm fraction probably indicates a slightly more disoriented particle organization for the coarser fraction. For the other fractions (*i.e.* 1−2 and 10−20 μm), the particle disorientation is more pronounced with increasing particle size, which is indicated by the increase in the proportion of the isotropic contribution and the strong decrease in the relative g1 proportion. This feature, which is rather counterintuitive, has also been observed by Hall *et al.* (1983) on a <2 μm fraction on the sole basis of broadening of Gaussian functions without noticeable variation in isotropic contribution. In the present study, the use of a wide range of particle sizes and the consideration of a coarser 10−20 μm fraction having overwhelming isotropic contribution further demonstrate the particle-size dependence of particle orientation (Figures 6, 7) and the increase in disorientation with size of particles. Note that such an evolution with the sizes of the particles appears fully logical with the 001 reflection intensities observed along the $q_{//}$ or $q_\perp$ directions in the 1D patterns; the increase of the cont$_{cst}$ value is correlated with the increase in the $q_{//}/q_\perp$ intensity ratio.

For a given particle-size fraction, the hydration state has been reported by Cebula *et al.* (1979) as having either a minor or no influence on the particle orientation. In the present study and despite the observed significant reduction in the macroscopic volume during dehydration for the <2 μm fractions, the results from the RC analysis do not display any significant trend (Table 2). Indeed, both the relative proportions and the widths of the different contributions remain similar irrespective of the hydration state, thus confirming the conclusions of Cebula *et al.* (1979) on montmorillonites saturated with monovalent cations. However, note that although the orientations of particles do not change, they encounter a significant uniaxial reduction in their thickness from ~30% when decreasing the hydration state, as observed from the decrease in the individual layer thicknesses from ~15 Å to ~10 Å in the 2W and 0W states, respectively (Figure 5, Table 1). Consequently, the lack of change in the particle orientation in the porous medium cannot preclude a change in the overall particles and the associated organization of the pore network. In this respect, information about the larger-scale morphology and possible changes in the hydration state can be best revealed by analyzing the SANS patterns.

Influence of particle orientation on SANS patterns

Influence on the slope determined from a log(I) vs. log(q) plot. The intensity in the small-angle region arises from heterogeneities or variations in the scattering-length density at a larger spatial scale compared to the diffraction angular region. Consequently, the SANS patterns obtained may be considered the result of the influence of the particle properties on a larger spatial scale (*i.e.* size, shape, and surfaces) and their organization in the clay media. Therefore, the intensity in the small-angle domain will be interpreted to arise from an assembly of anisometric particles, the scattering-length density of which may be considered a constant for all particles in the different size fractions.

In the small-angle scattering domain, the absolute intensity classically follows a power law as a function of q:

$$I(q) = k.q^{-m} \qquad (13)$$

where k is a coefficient related to the contrast and the proportion of the scattering moieties. To derive the values of m in the present case, the slope of the linear region in a log (I) *vs.* log (q) plot was estimated in the $0.029 < q < 0.109$ Å^{-1} range along the $q_{//}$ and $q_\perp$ directions and, after correction, from an incoherent background (Figure 4).

No clear evolution of the m values with hydration state for a given size fraction could be determined (Table 3). However, the exponents obtained for the different size fractions reveal various trends. First, the values of m obtained ranged between ~2 and 4, values which have

Table 3. Power law exponent, m, extracted from the 1D SANS patterns recorded in both the $q_{//}$ and $q_\perp$ directions.

Sample	Hydration state	m $(q_{//})$	m $(q_\perp)$
<0.1 μm	2W	3.21(3)	2.04(4) 2.72(3)
	0W	3.43(2)	2.84(2)
0.1−0.2 μm	2W	3.42(3)	2.80(3)
	1W	3.37(3)	3.15(1)
	0W	3.50(3)	3.11(1)
1−2 μm	2W	3.62(6)	3.42(3)
	1W	3.97(6)	3.91(3)
	0W	3.99(4)	3.94(3)
10−20 μm	2W	3.97(13)	3.79(8)
	1W	3.89(9)	3.52(5)
	0W	3.63(8)	3.33(4)

For the <0.1 μm fraction in the bihydrated state, two m values were extracted, in the $0.029 < q < 0.065$ and the $0.065 < q < 0.109$ Å^{-1} region, respectively. Values in parentheses represent standard deviation on the last digit.

been reported repeatedly in the case of porous clay media (Morvan *et al.*, 1994; Bihannic *et al.*, 2001; Knudsen *et al.*, 2004; Méheust *et al.*, 2007; Jin *et al.*, 2011). Second, the values of m obtained along the $q_{//}$ direction are systematically greater than those obtained along the $q_\perp$ direction. Third, an increase in the m values was observed for both the $q_{//}$ and $q_\perp$ directions when comparing the two finer (<0.1 or 0.1−0.2 μm) and the two coarser (1−2 or 10−20 μm) fractions. Finally, the difference between the power-law exponents obtained along the $q_{//}$ and $q_\perp$ directions for a given sample decreases for the two coarser fractions compared to the finer ones.

To better understand the evolution of the m values with the morphology and orientation of the particles, consider the theoretical expression for the intensity scattered by a population of monodisperse, non-interacting oriented objects (Guinier and Fournet, 1951):

$$I(\vec{q}) = K \int_0^{2\pi} \int_0^{\pi} \left[F(\vec{q}) \right]^2 g(\alpha) \sin(\alpha) d\alpha d\psi \qquad (14)$$

In this equation, the intensity is expressed as a function of the scattering vector, $\vec{q}$. K is an experimental constant, $g(\alpha)$ is the orientation distribution function, and the double integral corresponds to an averaging over all orientations. Finally, $F(\vec{q})$ is the form factor of the particles. For disk-shaped particles with a thickness of l and a radius of a, $F(\vec{q})$ is expressed as:

$$F(\vec{q}) = F(q, \gamma) = \frac{\sin(ql \cos \gamma/2)}{ql \cos \gamma/2} \frac{2 J_1 \sin(qa \sin \gamma)}{qa \sin \gamma} \qquad (15)$$

where γ represents the angle between the disk-axis, $\vec{n}$, and $\vec{q}$, and J_1 is the first-order Bessel function of the first type.

In the SANS configuration, one may consider that q lies in the detector plane (plane also defined by the two directions $q_\perp$ and $q_{//}$, on Figure 5b), and can, thus, be expressed relative to the angle φ, which is defined as the angle between q and the horizontal axis of the detector. In the present configuration, φ equals 0 and $\pi/2$ along the $q_\perp$ and $q_{//}$ directions, respectively. Therefore, all angles are related by the following relationship: $\cos\gamma = \cos\alpha\sin\varphi + \sin\alpha\cos\varphi\cos\psi$. Following the previous geometrical considerations (Lemaire *et al.*, 2002), equation 14 can be rewritten as:

$$I(\vec{q}) = I(q, \varphi) =$$

$$K \int_0^{2\pi} \int_0^{\pi} \left[\frac{\sin(ql\cos\gamma/2)}{ql\cos\gamma/2} \frac{2J_1\sin(qa\sin\gamma)}{qa\sin\gamma} \right]^2 g(\alpha)\sin(\alpha)d\alpha d\psi$$

$$(16)$$

Consequently, equation 13 describes the asymptotic behavior of equation 16. The value of m derived from the analysis of the slope of the $\log(I)$ *vs.* $\log(q)$ plot (Table 3) is related directly to both the form factor of particles $F(\vec{q})$ and the shape of the ODF $g(\alpha)$. An expression similar to equation 16 was used in a previous study to calculate the scattering patterns of infinitely thin disks under shear-flow conditions (Bihannic *et al.*, 2010). With an increasing degree of anisotropy, a greater shift was observed between the scattering curves calculated along the horizontal and vertical directions, which correspond to the $q_\perp$ and $q_{//}$ directions, respectively. In the present study, the increase in the difference between the m values in the two directions for the two smallest size fractions probably indicates an augmentation of the anisotropic properties of the system in the intermediate length scale probed by the SANS measurements.

To assess the influence of the form factor, $F(\vec{q})$, on the m values, consider first a purely isotropic system. In such a case, the scattered intensity varies as a function of q, but it is independent of the value of φ. This case would result in similar 1D SANS/ND curves along the $q_{//}$ and $q_\perp$ directions. For such an isotropic case, the intensity would decrease as q^{-2} for $q<(2\pi/l)$ and q^{-4} for $q>>(2\pi/l)$, *i.e.* in the Porod regime (Guinier and Fournet, 1951). In the present study, the values of m obtained along the $q_\perp$ direction increase progressively with increasing particle size, starting from a value close to 2 for the finest fraction to reach a value close to 4 for the coarsest one. In the latter case, one may consider in a first approximation that the Porod domain is reached, which indicates that the particle thickness is >216 Å ($l = 2\pi/q_{min} = 2\pi/0.029$). To verify this hypothesis, the size of the crystallites was estimated roughly by applying the Scherrer formula on the 001 diffraction peak for the

bihydrated samples. Note that for other hydration states, the presence of heterogeneous hydration states (Figure 4) precludes the use of this formula. On the basis of the Scherrer relation, the sizes of the coherent scattering domains were determined to be 140, 190, 310, and 300 Å for the <0.1, 0.1−0.2, 1−2, and 10−20 μm particles, respectively. For the two coarser fractions, this value is likely to be underestimated given the instrumental resolution. The size of the coherent scattering domains obtained confirms that the Porod regime is reached for the 1−2 and 10−20 μm fractions and may explain the m values of ~4 obtained for these fractions (Table 3). For the 0.1−0.2 μm size fraction, the thickness of the coherent scattering domain is on the same order of magnitude as the maximal length probed by SANS. In this particular case, the value of m close to 3 is probably due to the polydispersity of the system, which can be considered a mixture of particles, the individual signal of which would lie near 2 or 4 depending on their respective thicknesses (for thin and thick particles, respectively). As far as the <0.1 μm fraction is concerned, two m values with a crossover located for q near 0.065 Å^{-1} were obtained. Such a crossover corresponding to a thickness of 97 Å is in rather good agreement with the thickness of the coherent scattering domains (140 Å) determined from the Scherrer relation. From the previous analysis, the qualitative interpretation of the evolution of m values with particle size is, thus, consistent with the increase in particle thickness and with the presence of a more isotropic organization for the coarser fractions.

Influence on the shape of the central halo. Additional information about the isotropic/anisotropic features of the particles and the crystal−pore interfaces can be obtained by examining the two-dimensional SANS/ND patterns (Figure 8). Again, no change in the shape of the central halo was observed as a function of the hydration state for a given sample. In contrast, significant changes were observed when comparing the different particle size fractions. For the finest <0.1 and 0.1−0.2 μm size fractions, the elliptic shapes also indicate an anisotropic organization of the material, whereas the circular pattern observed for the coarsest 10−20 μm fraction suggests an isotropic system (Lemaire *et al.*, 2002; Knudsen *et al.*, 2004; Itakura *et al.*, 2005; Bihannic *et al.*, 2010; Jin *et al.*, 2011). The 2D SANS patterns can also be used to extract orientation functions for the different size fractions (Figure 9a). This process was performed through azimuthal integration over φ for $q = 0.038$ Å^{-1} on dehydrated specimens to limit additional uncertainty due to incoherent signal correction. The probability density functions ($N_{SA}(\varphi)$) were calculated as follows (Figure 9a):

$$N_{SA}(\varphi) = I_{q=0.038}(\varphi) / \int_0^{\pi} I_{q=0.038}(\varphi) 2\pi\sin(\varphi)d\varphi \quad (17)$$

$q_\perp$

<0.1 µm

2W

0W

0.1-0.2 µm
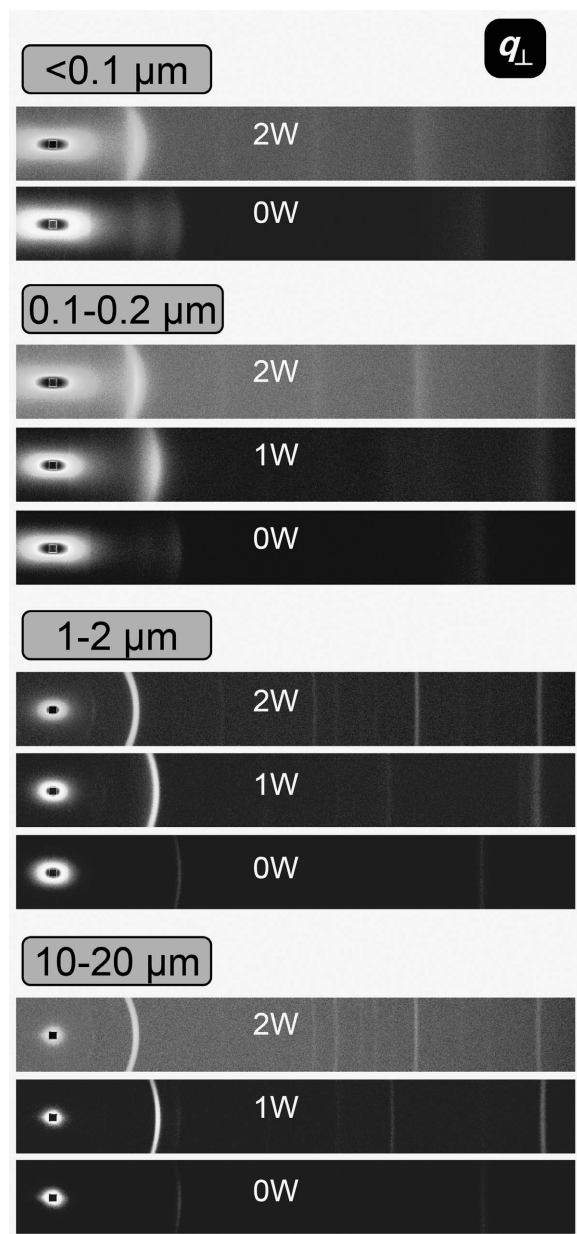
2W

1W

0W

1-2 µm

2W

1W

0W

10-20 µm

2W

1W

0W

Figure 8. 2D small-angle/neutron diffraction patterns obtained in the $q_\perp$ direction for the different particle size fractions in the bihydrated (2W), monohydrated (1W), and dehydrated (0W) states.

These functions display similar features for the two finest fractions, whereas a noticeable decrease in magnitude and a broadening of the principal maxima are observed for the coarser ones. Such features further support the increase of isotropy with the size of the particles and can be viewed as a remnant of the particle orientation characterization performed above. Indeed, the comparison between the orientation functions extracted from the SANS patterns and those derived from the RC treatment (Figure 9b) display a logical

evolution with particle size. In the case of fine fractions, the particles display an anisotropic organization because they have a strong tendency to lie flat on the sedimentation plane. With increasing size fractions, the particles tend to display a more isotropic organization (Table 2). This more random organization, in turn, results in the presence of more isotropic features irrespective of the observation scale, leading, for the coarsest (10–20 µm) fraction, to closer scattered intensities and m values in the $q_\perp$ and $q_{//}$ directions (Figure 5, Table 3) as well as a circular central halo on a 2D SANS image (Figure 8) and an almost flat orientation function in the small-angle region (Figures 8, 9).

Note that if both orientation functions derived from the RC and SANS analyses display similar features, they do not match in width and intensity (Figure 9b). Indeed, for all fractions, the orientation functions derived from the SANS images exhibit characteristics of less anisotropic systems compared to those derived from the RC treatment. Because $g(\alpha)$ in equation 16 corresponds to the $N_e(\alpha)$ derived from the RC treatment, the deviation between $N_{SA}(\varphi)$ and $N_e(\alpha)$ obtained can be assigned to the influence of the form factor, $F(\vec{q})$ (including particle sizes, shapes, and surfaces). This influence does not allow further treatment of the $N_{SA}(\varphi)$ curves, as performed here for the experimental RCs, without additional information about the actual morphology of the particles and about the contribution of the particle–pore interfaces. A theoretical reconstruction of the experimental SANS/ND patterns, based on the morphological properties of the particles in these different size fractions, is necessary, therefore, to address fully the quantitative correlation between the particles and the crystal–pore interface orientation functions.

CONCLUSIONS

The characterization of the particle orientations and their associated crystal–pore interfaces in different synthetic porous media prepared from selected particle size fractions of vermiculite allows three major conclusions to be derived.

First, from the analyses of the RC data, quantitative particle orientation distributions have been obtained for the different particle size fractions. The fitting strategy adopted, which assumes Gaussian distributions and one flat background similar to that proposed by Cebula et al. (1979) and Hall et al. (1983), allows description of the full set of experimental RCs in the $q_\perp$ direction. Furthermore, the isotropic nature of the flat contribution previously suggested in the literature is demonstrated by using the present experimental set up with RC analyses in both $q_{//}$ and $q_\perp$. Indeed, this contribution is quantitatively similar in both the $q_{//}$ and the $q_\perp$ directions and highlighted qualitatively on experimental RCs obtained for the coarsest size fractions. Therefore, by taking into account both isotropic and anisotropic
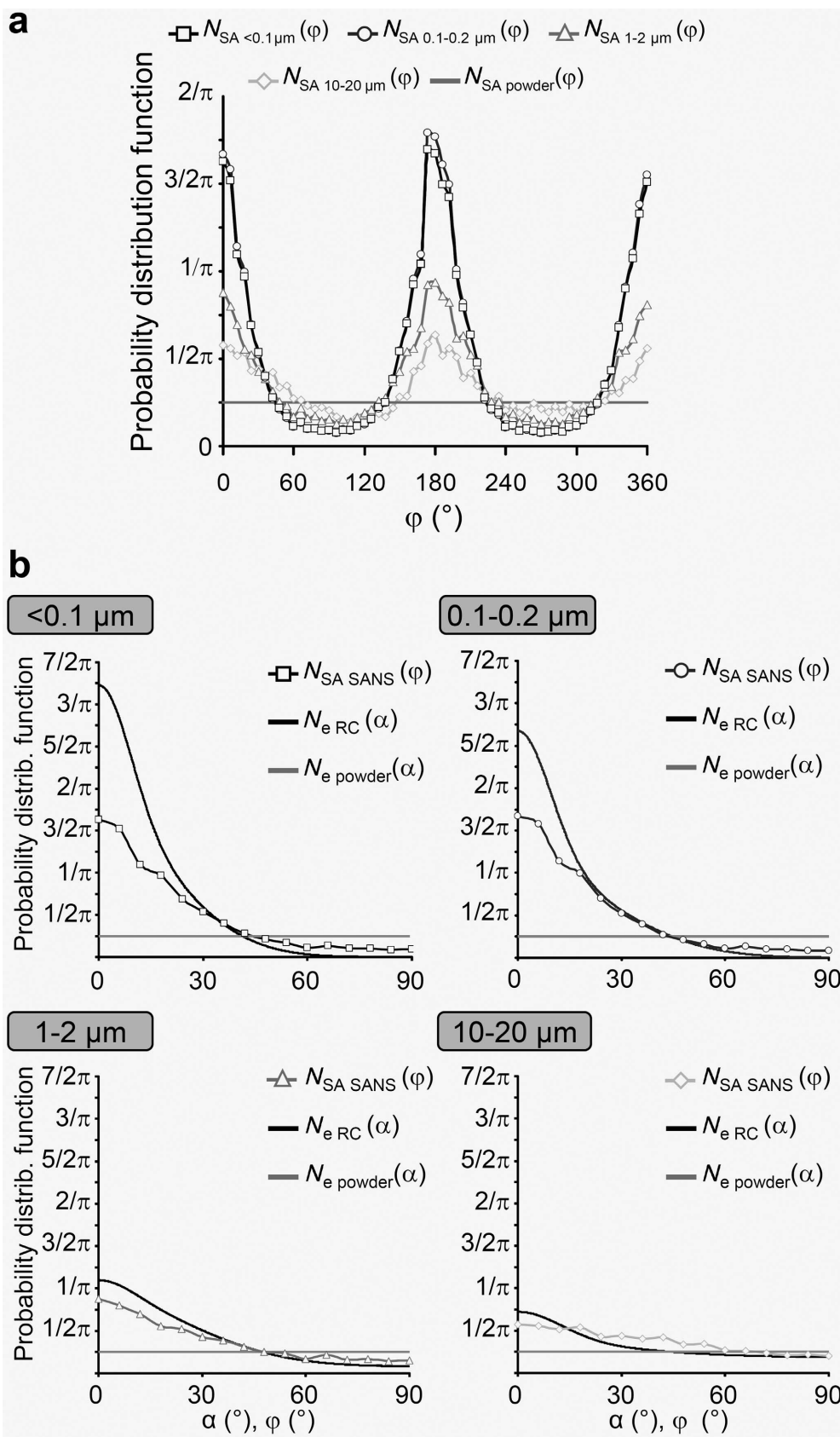
contributions, the effect of particle size on their mutual arrangement can be assessed. As compared to existing studies, the range of particle sizes and degree of orientation is extended, which allows the characterization of quasi-isotropic porous media. As far as the authors are aware, this has never been described for swelling clay porous media prepared by sedimentation. For the finest particle sizes, the experimental RCs obtained in the present study for vermiculite are similar to those described for montmorillonite with similar size fractions (Cebula *et al.*, 1979; Hall *et al.*, 1983). This preliminary result can be assigned tentatively to a minor or zero influence of the layer charge and charge location (octahedral *vs*. tetrahedral) on the anisotropic features of the swelling clay porous media. In contrast, the results obtained further confirm the previous interpretation on the overwhelming influence of the particle size on their orientational properties. The general tendency of decreasing anisotropy when increasing particle size is rather counterintuitive. Information derived from the numerical modeling of the particle sedimentation indicates that only a significant change in the aspect ratio (lateral/thickness dimensions of particle) could result in such a variation in the particle orientation (Zou and Yu, 1996; Coelho *et al.*, 1997). Further studies, including morphological characterization of the particles, are required to assess this hypothesis. The determination of the morphological features of the particles in addition to their quantitative orientational properties, as performed in the present study, might provide experimental constraints to help in assessing the robustness of numerical sedimentation models for reproducing natural and/or synthetic systems.

Second, in agreement with the existing literature (Cebula *et al.*, 1979; Méheust *et al.*, 2007), the present study indicates that the hydration state has a negligible impact on the organization of the porous media for platy swelling clays, despite the noticeable change in the macroscopic volume of the sample. The present study is devoted to the dehydration process in free shrinking conditions, whereas the results from Devineau *et al.* (2006) were obtained in a confined swelling environment and revealed a different behavior. Indeed, during the hydration process, these authors demonstrated a partial reorientation of the clay particles under confined conditions compared to the free swelling case. Therefore, further investigations could include a

characterization of the influence of confinement on these samples.

Third, qualitative analysis of the experimental SANS 2D patterns reveals consistent results concerning the larger-scale morphology associated with the particle orientation. Indeed, anisotropy features in the 2D patterns are in agreement with the analysis of the rocking curves (Figure 8 (Lemaire *et al.*, 2002; Knudsen *et al.*, 2004; Méheust *et al.*, 2007; Jin *et al.*, 2011)). Calculating theoretical SANS patterns and comparing them with the experimental data obtained here would undoubtedly provide new insights for a quantitative correlation between the particles and the orientation distributions of crystal−pore interfaces. In addition, such an approach would help in better interpreting the m values obtained and their evolution with particle size and hydration state. This work could also benefit from a complete morphological characterization of the particle size and distribution, as mentioned above, and from additional SANS data obtained at lower q values, especially for the coarsest fractions (1−2 μm and 10−20 μm fractions).

ACKNOWLEDGMENTS

REFERENCES

Arguelles, A., Leoni, M., Blanco, J.A., and Marcos, C. (2010) Semi-ordered crystalline structure of the Santa Olalla vermiculite inferred from X-ray powder diffraction. *American Mineralogist*, **95**, 126−134.

Bihannic, I., Tchoubar, D., Lyonnard, S., Besson, G., and Thomas, F. (2001) X-ray scattering investigation of swelling clay fabric. 1− the dry state. *Journal of Colloid and Interface Science*, **240**, 211−218.

Bihannic, I., Delville, A., Deme, B., Plazanet, M., Villieras, F., and Michot, L.J. (2009) Clay swelling: New insights from neutron-based techniques. Pp. 521−546 in: *Neutron Applications in Earth, Energy and Environmental Sciences* (L. Liyuan, R. Rinaldi, and H. Schober, editors). Springer, Berlin.

Bihannic, I., Baravian, C., Duval, J.F.L., Paineau, E., Meneau, F., Levitz, P., de Silva, J.P., Davidson, P., and Michot, L.J. (2010) Orientational order of colloidal disk-shaped particles under shear flow conditions: a rheological-small-angle X-ray scattering study. *Journal of Physical Chemistry B*, **114**, 16347−16355.

Brunauer, S., Emmett, P.H., and Teller, E. (1938) Adsorption of gases in multimolecular layers. *Journal of the American Chemical Society*, **60**, 309−319.

Caillaud, J., Proust, D., Philippe, S., Fontaine, C., and Fialin,

Figure 9 (*facing page*). Comparison of dehydrated samples between orientation distribution functions determined in the small-angle region ($N_{SA}(\varphi)$) and from rocking-curve analysis ($N_c(\alpha)$). (a) Evolution of the orientation distribution functions in the small-angle region ($q = 0.038$ Å^{-1}) for the different particle-size fractions. (b) Comparison between the orientation distribution functions shown in (a) and those obtained from the analysis of the experimental RCs.

M. (2009) Trace metals distribution from a serpentinite weathering at the scales of the weathering profile and its related weathering microsystems and clay minerals. *Geoderma*, **149**, 199−208

Cebula, D.J., Thomas, R.K., Middleton, S., Ottewill, R.H., and White, J.W. (1979) Neutron-diffraction from clay-water systems. *Clays and Clay Minerals*, **27**, 39−52.

Coelho, D., Thovert, J.F., and Adler, P.M. (1997) Geometrical and transport properties of random packings of spheres and aspherical particles. *Physical Review E: Statistical, Nonlinear, and Soft Matter Physics*, **55**, 1959−1978.

Czurda, K. (2006) Clay liners and waste disposal. Pp. 693−702 in: *Handbook of Clay Science* (F. Bergaya, B.K.G. Theng, and G. Lagaly, editors). Elsevier, Amsterdam.

de Haro, M.C.J., Perez-Rodriguez, J.L., Poyato, J., Perez-Maqueda, L.A., Ramirez-Valle, V., Justo, A., Lerf, A., and Wagner, F.E. (2005) Effect of ultrasound on preparation of porous materials from vermiculite. *Applied Clay Science*, **30**, 11−20.

de la Calle, C., Pezerat, H., and Gasperin, M. (1977) Problèmes d'ordre désordre dans les vermiculites-structure du minéral calcique hydraté à 2 couches. *Journal de Physique*, **38**, 128−133.

de la Calle, C., Suquet, H., Dubernat, J., and Pezerat, H. (1978) Mode d'empilement des feuillets dans les vermiculites hydratées à 'deux couches'. *Clay Minerals*, **13**, 275−297.

de la Calle, C., Suquet, H., and Pezerat, H. (1985) Vermiculites hydratées à une couche. *Clay Minerals*, **20**, 221−230.

de la Calle, C. and Suquet, H. (1988) Vermiculite. Pp. 455−496 in: *Hydrous Phyllosilicates (Exclusive of Micas)* (S.W. Bailey, editor). Mineralogical Society of America, Washington, D.C., USA.

Devineau, K., Bihannic, I., Michot, L., Villieras, F., Masrouri, F., Cuisinier, O., Fragneto, G., and Michau, N. (2006) In situ neutron diffraction analysis of the influence of geometric confinement on crystalline swelling of montmorillonite. *Applied Clay Science*, **31**, 76−84.

Dixon, J.B. and Weed, S.B. (1989) *Minerals in Soil Environments*. Soil Science Society of America Inc., USA, Madison, Wisconsin, USA.

Dohrmann, R., Ruping, K.B., Kleber, M., Ufer, K., and Jahn, R. (2009) Variation of preferred orientation in oriented clay mounts as a result of sample preparation and composition. *Clays and Clay Minerals*, **57**, 686−694.

Drits, V.A. and Tchoubar, C. (1990) *X-ray Diffraction by Disordered Lamellar Structures: Theory and Applications to Microdivided Silicates and Carbons*. Springer-Verlag, Berlin.

Drits, V.A., Środoń, J., and Eberl, D.D. (1997) XRD measurement of mean crystallite thickness of illite and illite/smectite: Reappraisal of the Kübler index and the Scherrer equation. *Clays and Clay Minerals*, **45**, 461−475.

Ferrage, E., Lanson, B., Malikova, N., Plançon, A., Sakharov, B.A., and Drits, V.A. (2005a) New insights on the distribution of interlayer water in bi-hydrated smectite from X-ray diffraction profile modeling of 00l reflections. *Chemistry of Materials*, **17**, 3499−3512.

Ferrage, E., Lanson, B., Sakharov, B.A., and Drits, V.A. (2005b) Investigation of smectite hydration properties by modeling of X-ray diffraction profiles. Part 1. Montmorillonite hydration properties. *American Mineralogist*, **90**, 1358−1374.

Ferrage, E., Lanson, B., Michot, L.J., and Robert, J.L. (2010) Hydration properties and interlayer organization of water and ions in synthetic Na-smectite with tetrahedral layer charge. Part 1. Results from X-ray diffraction profile modeling. *Journal of Physical Chemistry C*, **114**, 4515−4526.

Ferrage, E., Sakharov, B.A., Michot, L.J., Delville, A., Bauer, A., Grangeon, S., Frapper, G., Jimenez-Ruiz, M., and Cuello, G.J. (2011) Hydration properties and interlayer organization of water and ions in synthetic Na-smectite with tetrahedral layer charge. Part 2. Towards a precise coupling between molecular simulations and diffraction data. *Journal of Physical Chemistry C*, **115**, 1867−1881.

González García, F. and García Ramos, G. (1960) On the genesis and transformations of vermiculite. Pp. 482−491 in: *Transactions of the 7th International Congress on Soil Science*, **4**, CABI, Oxfordshire, UK

Guinier, A. and Fournet, G. (1951) *Small-angle Scattering of X-rays*. John Wiley & Sons, New York.

Hall, P.L., Harrison, R., Hayes, M.H.B., Tuck, J.J., and Ross, D.K. (1983) Particle orientation distributions and stacking arrangements in size-fractionated montmorillonite measured by neutron and X-ray diffraction. *Journal of the Chemical Society, Faraday Transactions 1: Physical Chemistry in Condensed Phases*, **79**, 1687−1700.

Harris, G.L., Nicholls, P.H., Bailey, S.W., Howse, K.R., and Mason, D.J. (1994) Factors influencing the loss of pesticides in drainage from a cracking clay soil. *Journal of Hydrology*, **159**, 235−253.

Harvey, C.C. and Lagaly, G. (2006) Conventional applications. Pp. 501−540 in: *Handbook of Clay Science* (F. Bergaya, B.K.G. Theng, and G. Lagaly, editors). Elsevier, Amsterdam.

Hubert, F., Caner, L., Meunier, A., and Ferrage, E. (2012) Unraveling complex <2 μm clay mineralogy from soils using X-ray diffraction profile modeling on particle-size sub-fractions: Implications for soil pedogenesis and reactivity. *American Mineralogist*, **97**, 384−398.

Inigo, A.C., Tessier, D., and Pernes, M. (2000) Use of X-ray transmission diffractometry for the study of clay-particle orientation at different water contents. *Clays and Clay Minerals*, **48**, 682−692.

Itakura, Y., Bertram, W.K., and Knott, R.B. (2005) The nanoscale structural response of natural kaolinite clayey soil subjected to uniaxial compression. *Applied Clay Science*, **29**, 1−14.

Jin, L.X., Rother, G., Cole, D.R., Mildner, D.F.R., Duffy, C.J., and Brantley, S.L. (2011) Characterization of deep weathering and nanoporosity development in shale − a neutron study. *American Mineralogist*, **96**, 498−512.

Johansen, T.A., Jakobsen, M., and Ruud, B.O. (2002) Estimation of the internal structure and anisotropy of shales from borehole data. *Journal of Seismic Exploration*, **11**, 363−381.

Johansen, T.A., Ruud, B.O., and Jakobsen, M. (2004) Effect of grain scale alignment on seismic anisotropy and reflectivity of shales. *Geophysical Prospecting*, **52**, 133−149.

Knudsen, K.D., Fossum, J.O., Helgesen, G., and Haakestad, M.W. (2004) Small-angle neutron scattering from a nano-layered synthetic silicate. *Physica B − Condensed Matter*, **352**, 247−258.

Lemaire, B.J., Panine, P., Gabriel, J.C.P., and Davidson, P. (2002) The measurement by SAXS of the nematic order parameter of laponite gels. *Europhysics Letters*, **59**, 55−61.

Lonardelli, I., Wenk, H.-R., and Ren, Y. (2007) Preferred orientation and elastic anisotropy in shales. *Geophysics*, **72**, D33−D40.

Marcos, C., Argüelles, A., Ruíz-Conde, A., Sánchez-Soto, P.J., and Blanco, J.A. (2003) Study of the dehydration process of vermiculites by applying a vacuum pressure: Formation of interstratified phases. *Mineralogical Magazine*, **67**, 1253−1268.

Méheust, Y., Knudsen, K.D., and Fossum, J.O. (2006) Inferring orientation distributions in anisotropic powders of nano-layered crystallites from a single two-dimensional WAXS image. *Journal of Applied Crystallography*, **39**, 661−670.

Méheust, Y., Dagois-Bohy, S., Knudsen, K.D., and Fossum, J.O. (2007) Mesoscopic structure of dry-pressed clay samples from small-angle X-ray scattering measurements. *Journal of Applied Crystallography*, **40**, 286–291.

Méring, J. (1949) L'interférence des rayons-x dans les systèmes à stratification désordonnée. *Acta Crystallographica*, **2**, 371–377.

Montarges-Pelletier, E., Bogenez, S., Pelletier, M., Razafitianamaharavo, A., Ghanbaja, J., Lartiges, B., and Michot, L.J. (2005) Synthetic allophane-like particles: Textural properties. *Colloids and Surfaces A: Physicochemical and Engineering Aspects*, **255**, 1–10.

Morvan, M., Espinat, D., Lambard, J., and Zemb, T. (1994) Ultrasmall-angle and small-angle X-ray-scattering of smectite clay suspensions. *Colloids and Surfaces A − Physicochemical and Engineering Aspects*, **82**, 193–203.

Perdigon-Aller, A.C., Aston, M., and Clarke, S.M. (2005) Preferred orientation in filtercakes of kaolinite. *Journal of Colloid and Interface Science*, **290**, 155–165.

Perdigon, A.C., Clarke, S.M., and Aston, M. (2007) Neutron diffraction study of the orientational order in filter cakes made of kaolinite under laminar and turbulent cross-flow. *Journal of Membrane Science*, **298**, 80–91.

Perez-Maqueda, L.A., Caneo, O.B., Poyato, J., and Perez-Rodriguez, J.L. (2001) Preparation and characterization of micron and submicron-sized vermiculite. *Physics and Chemistry of Minerals*, **28**, 61–66.

Perez-Maqueda, L.A., De Haro, M.C.J., Poyato, J., and Perez-Rodriguez, J.L. (2004) Comparative study of ground and sonicated vermiculite. *Journal of Materials Science*, **39**, 5347–5351.

Plançon, A. (1980) The calculation of intensities diffracted by a partially oriented powder with a layer structure. *Journal of Applied Crystallography*, **13**, 524–528.

Prêt, D., Sammartino, S., Beaufort, D., Fialin, M., Sardini, P., Cosenza, P., and Meunier, A. (2010a) A new method for quantitative petrography based on image processing of chemical element maps: Part II. Semi-quantitative porosity maps superimposed on mineral maps. *American Mineralogist*, **95**, 1389–1398.

Prêt, D., Sammartino, S., Beaufort, D., Meunier, A., Fialin, M., and Michot, L.J. (2010b) A new method for quantitative petrography based on image processing of chemical element maps: Part I. Mineral mapping applied to compacted bentonites. *American Mineralogist*, **95**, 1379–1388.

Reynolds, R.C. (1986) The Lorentz-polarization factor and preferred orientation in oriented clay aggregates. *Clays and Clay Minerals*, **34**, 359–367.

Ross, D.K. and Hall, P.L. (1980) Neutron scattering methods of investing clay systems. Pp. 93–163 in: *Advanced Chemical Methods for Soil and Clay Minerals Research* (J.W. Stucki and W.L. Banwart, editors). D. Reidel Publishing Company, Boston, USA.

Tertre, E., Ferrage, E., Bihannic, I., Michot, L.J., and Pret, D. (2011a) Influence of the ionic strength and solid/solution ratio on Ca(II)-for-Na$^+$ exchange on montmorillonite. Part 2: Understanding the effect of the m/v ratio. Implications for pore water composition and element transport in natural media. *Journal of Colloid and Interface Science*, **363**, 334–347.

Tertre, E., Pret, D., and Ferrage, E. (2011b) Influence of the ionic strength and solid/solution ratio on Ca(II)-for-Na$^+$ exchange on montmorillonite. Part 1: Chemical measurements, thermodynamic modeling and potential implications for trace elements geochemistry. *Journal of Colloid and Interface Science*, **353**, 248–256.

Tertre, E., Hubert, F., Bruzac, S., Pacreau, M., Ferrage, E., and Prêt, D. (2013) Ion-exchange reactions on clay minerals coupled with advection/dispersion processes. Application to Na$^+$/Ca^{2+} exchange on vermiculite: Reactive-transport modeling, batch and stirred flow-through reactor experiments. *Geochimica et Cosmochimica Acta*, **112**, 1–19.

Tessier, D., Bouzigues, B., Favrot, J.C., and Valles, V. (1992) Influence of decimetric microrelief on clay texture evolution of hydromorphic soils of the Garonne river − differentiation of vertical and prismatic structures. *Comptes Rendus de L'Academie des Sciences Serie II*, **315**, 1027–1032.

Vasseur, G., Djeranmaigre, I., Grunberger, D., Rousset, G., Tessier, D., and Velde, B. (1995) Evolution of structural and physical parameters of clays during experimental compaction. *Marine and Petroleum Geology*, **12**, 941–954.

Voltolini, M., Wenk, H.R., Mondol, N.H., Bjorlykke, K., and Jahren, J. (2009) Anisotropy of experimentally compressed kaolinite-illite-quartz mixtures. *Geophysics*, **74**, 13–23.

Wiewióra, A., Pérez-Rodríguez, J.L., Perez-Maqueda, L.A., and Drapala, J. (2003) Particle size distribution in sonicated high- and low-charge vermiculites. *Applied Clay Science*, **24**, 51–58.

Zou, R.P. and Yu, A.B. (1996) Evaluation of the packing characteristics of mono-sized non-spherical particles. *Powder Technology*, **88**, 71–79.